Angle dependence of strong-field single and double ionization of carbonyl sulfide

Péter Sándor,[1,*] Adonay Sissay,[2] François Mauger,[3] Paul M. Abanador,[3] Timothy T. Gorman,[4] Timothy D. Scarborough,[4] Mette B. Gaarde,[3] Kenneth Lopata,[2,5] Kenneth J. Schafer,[3] and Robert R. Jones[1]

[1]*Department of Physics, University of Virginia, Charlottesville, Virginia 22904, USA*
[2]*Department of Chemistry, Louisiana State University, Baton Rouge, Louisiana 70803, USA*
[3]*Department of Physics and Astronomy, Louisiana State University, Baton Rouge, Louisiana 70803, USA*
[4]*Department of Physics, The Ohio State University, Columbus, Ohio 43210, USA*
[5]*Center for Computation and Technology, Louisiana State University, Baton Rouge, Louisiana 70808, USA*

(Received 1 July 2018; published 17 October 2018)

We have studied, experimentally and theoretically, the ionization probability of carbonyl sulfide (OCS) molecules in intense linearly polarized 800-nm laser pulses as a function of the angle between the molecular axis and the laser polarization. Experimentally, the molecules are exposed to two laser pulses with a relative time delay. The first, weaker pulse induces a nuclear rotational wave packet within each molecule such that the ensemble exhibits preferential alignment in the laboratory frame at specific times. The second, stronger pulse induces ionization, and the variation in single and double ionization yields is measured as a function of the delay between the two pulses. The angular dependence of the ionization yield is extracted by fitting the delay-dependent yields to a sum of delay-dependent moments of the rotational wave packet's angular distribution. We compute these same angular-dependent strong-field ionization yields for OCS using time-dependent density-functional theory (TDDFT). For the single-ionization case, our measurements agree well with TDDFT calculations and with previous experiments. Furthermore, analysis of the simulated one-body density reveals that, when averaged over a laser cycle, the resulting hole is delocalized across the molecule for light polarized perpendicular to the molecular axis and mostly localized on the sulfur for parallel polarization. This suggests that preferential molecular alignment is a key parameter for controlling charge migration dynamics initiated by strong-field ionization. For double ionization, the agreement between experiment and theory is less compelling, reflecting the substantial challenges of computing double-ionization yields using TDDFT methods.

DOI: 10.1103/PhysRevA.98.043425

I. INTRODUCTION

Ionization provides the critical first step in many strong-field processes of current interest, from high-harmonic generation and attosecond pulse generation to laser-induced electron diffraction for time-resolved molecular imaging [1–7]. For molecules exposed to intense low-frequency fields, the single- and multiple-ionization rates can depend critically on the alignment or orientation of the molecule relative to the direction of the applied field at the instant of ionization [8–19]. Moreover, this relative alignment or orientation influences the degree to which various molecular orbitals contribute to the ionization process and determines the subsequent coherent hole dynamics in the molecular ion. As such, the ability to control molecular alignment or orientation in the laboratory and accurately simulate the collective electronic response to the intense laser are critical capabilities for exploring ultrafast electronic processes in molecules. Together, these might enable the use of strong-field ionization as a trigger for initiating fast electron motion within molecules and for observing or controlling the ensuing correlated dynamics. Here we describe measurements of intensity- and angle-dependent strong-field ionization of carbonyl sulfide (OCS) that test calculations which, in addition to predicting the ionization yields, provide insight into hole dynamics that are not observable in the current experiments.

Carbonyl sulfide is a particularly useful molecule for our combined experimental and theoretical studies for several reasons. First, accurate single-ionization anisotropy measurements utilizing well-characterized adiabatically and nonadiabatically aligned molecules are already available for OCS [13,18]. Therefore, we are able to test the accuracy of a different method for extracting ionization yield anisotropies against independent single-ionization measurements. Second, previous calculations have not been particularly successful in reproducing the OCS single-ionization measurements at 800 nm [13], providing a challenge for our theoretical approach. Third, just above the 800-nm single-ionization saturation intensity, the primary double-ionization channel is nondissociative and its angular dependence has not been reported. Thus, our double-ionization measurements provide additional insight and exacting tests of theory.

As alluded to above, strong-field ionization in molecules is a challenging problem for first-principles theory, as it requires a proper description of many-electron correlation effects. From a simulation standpoint, a variety of computational approaches have been applied to angle-dependent ionization rates in molecules [8,12–20]. These range from orbital model-based approaches like molecular-orbital Ammosov-

*ps5at@virginia.edu

Delone-Krainov (MOADK) theory [21–23] and weak-field asymptotic theory [15,24–26] to first-principles methods such as time-dependent Hartree-Fock theory [27–29], time-dependent density-functional theory (TDDFT) [30–42], and time-dependent configuration-interaction singles [43–45].

Here we adapt the methodology of Sissay *et al.* [41] to compute strong-field single and double ionization of OCS. Our approach uses real-time TDDFT with atom-centered Gaussian-type orbitals [41,46–52], tuned range-separated hybrid (RSH) exchange-correlation functionals, and complex absorbing potentials (CAPs) to absorb the outgoing electron flux. All calculations are performed using a modified development version of NWCHEM [53]. In the context of strong-field ionization, RSH functionals have many advantages over conventional density-functional theory functionals, including reduced self-interaction errors, improved ionization potentials, and the correct asymptotic form of the Coulomb potential. Through analysis of the one-body density provided by TDDFT, we extract the single- and double-ionization contributions via the norm, as well as the localization of the hole resulting from strong-field ionization.

Our intensity- and angle-dependent single- and double-ionization yield measurements in OCS provide sensitive tests of our specific TDDFT approach and, by extension, of the nonperturbative electron and hole dynamics predicted by the simulations. Calculating double ionization is considerably more challenging than single ionization, due to possible contributions from multiple ionic orbitals (dissociative and nondissociative), coherent hole motion, and nonsequential ionization effects. Thus, our double-ionization measurements serve as an additional, deeper test of theory.

Distinct from many previous experiments [9–11,13,18], our angle-dependent ionization measurements in OCS do not rely on independent experimental characterization of the molecular angular distribution in the target ensemble and are not explicitly limited by imperfect alignment. Instead, we take advantage of the fact that for a low-density ensemble of (nearly) rigid rotors, in experiments where the rotational temperature and aligning laser intensity are reasonably well defined, the time dependence of the molecular angular probability distribution can be accurately calculated from well-known molecular constants and a few key experimental parameters [10,11,54,55]. We employ transient alignment in a pump-probe scheme and measure the variation in the single- and double-ionization yields as a function of delay between the nonionizing alignment and more intense ionization pulses. The delay-dependent yields are then fit to moments of the calculated delay-dependent rotational distributions [19,56]. The fitted coefficients of those moments define the angle-dependent ionization probabilities.

In the following sections we first describe the experimental and analysis methods and present the extracted angle-dependent yields for single and double ionization of OCS. We then discuss the TDDFT approach and compare the calculated and measured results. For single ionization below the saturation intensity, we find that the angular dependence is in good agreement with previous measurements [13] and is fairly insensitive to ionizing field strength. As expected, above the saturation intensity ionization depletion of the molecular ensemble results in a nearly isotropic single-ionization yield. The intensity dependence of the measured single-ionization yield is well reproduced by the TDDFT calculations. On the other hand, above the single-ionization saturation intensity, the double-ionization yield shows a pronounced angular dependence which is not qualitatively captured by the calculations. Finally, we introduce a method for computing the localization of the hole following strong-field single ionization based on Bader charge [57–60] analysis of the time-dependent density. This analysis reveals the localization of the hole as a function of orientation, which is a crucial property for future charge migration studies.

II. EXPERIMENTAL APPROACH

The experiments utilize a multipass Ti:sapphire amplifier with a maximum pulse energy of 1.2 mJ and an 800-nm central wavelength. A beam splitter produces alignment (i.e., pump) and ionization (i.e., probe) pulses with nearly equal energy, and the relative delay between alignment and ionization pulses is controlled using a mechanical translation stage. The diameter of the alignment beam is reduced by a factor of $\sim$2 using a combination of a telescope and an iris. This ensures that, when focused in the interaction region, it has a larger diameter and a roughly constant intensity throughout the volume of molecules ionized by the probe. The iris also allows us to adjust the focused intensity of the alignment pulse so that it produces no measurable ionization. A Pockels-cell and a Glan-laser polarizer inserted into the alignment beam allows us to programmatically, and rapidly, toggle it on and off for accurate normalization of aligned to unaligned ionization yields. Immediately before entering the experimental vacuum chamber, the two pulses propagate parallel to each other (but not collinearly) with parallel linear polarization and pass through a single 250-mm-focal-length fused silica lens that ultimately focuses them into the target. Frequency-resolved optical gating (FROG) [61] measurements determine the duration of the alignment and ionization pulses after the lens to be 75 and 37 fs, respectively.

The alignment and ionization beams enter a high-vacuum chamber with a base pressure of 5×10^{-9} Torr and are focused to a common spot in a pulsed, supersonic molecular beam. The laser and molecular beams cross at a right angle. The molecular beam consists of a mixture of OCS in He buffer and originates in an Even-Lavie valve backed with a mixture pressure of 70–90 bars. The OCS concentration is kept low (500 ppm) to avoid clustering. The molecular beam passes through a skimmer which is several thousand nozzle diameters away from the interaction region. The OCS molecules are cooled during the supersonic expansion to a rotational temperature of 5–15 K, as estimated from fits of the measured ionization yields to moments of the delay-dependent rotational distribution of the OCS molecules (see Sec. III). The molecular beam has a diameter of $\sim$2 mm in the interaction region, well within the Rayleigh length of the focused alignment and ionizing laser beams.

A static voltage applied to two electric-field plates straddling the laser-molecule interaction region accelerates any positively charged ions produced by strong-field ionization toward a dual microchannel plate detector. Before reaching the detector, the ions pass through a field-free region with a

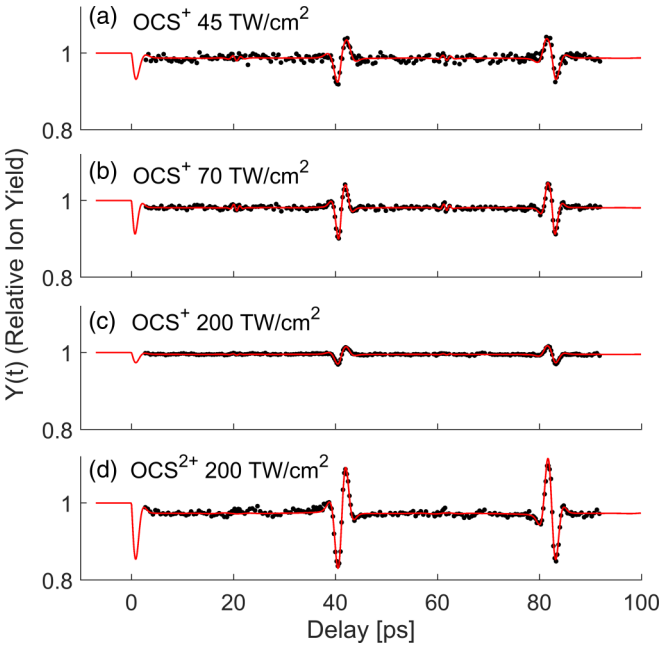

FIG. 1. Normalized ion yields $Y(t)$ for different ionization laser intensities and different ion charge states vs alignment-ionization pulse delay. Black data points are measurements and red curves are the best fits to the data as described in the text. The vertical scales are identical in each plot. The ionization intensities are calibrated as described in the text.

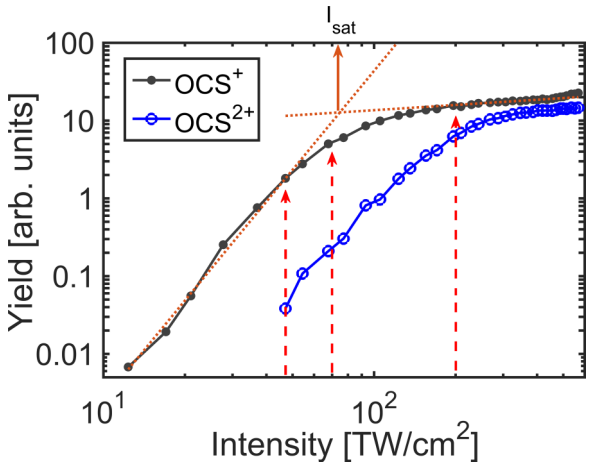

FIG. 2. The OCS^+ and OCS^{2+} yield vs ionizing laser intensity for an unaligned OCS target. The vertical red dashed arrows show the intensities at which the data in Fig. 1 were collected. The brown dashed lines show the fits to the pre- and postsaturation slopes. The brown solid arrow shows the extracted saturation intensity for the data set. The intensity axis is calibrated as described in the text.

length of approximately 20 cm. After each laser shot, ions striking the microchannel plate produce a time-dependent voltage on the detector anode which is out-coupled through a capacitor, amplified, and then digitized by an eight-bit high-speed PCI digitizer (Agilent Acqiris U1071A). The voltage level in each time bin is summed over 100 laser shots at a fixed alignment-ionization pulse delay, producing the time-of-flight (TOF) trace for that delay. Within the digitized TOF traces, peaks corresponding to singly and (if present) doubly charged OCS parent ions are boxcar integrated during postprocessing to obtain the ion yield for each species as a function of delay. The Pockels cell in the alignment beam toggles the alignment beam on and off every 100 laser shots, allowing us to eliminate drifts in the OCS concentration by normalizing the aligned ion yields to unaligned yields at 100-ms time intervals. The normalized ion yields from 100 to 200 delay scans are combined to obtain the delay-dependent normalized ion yield $Y(t)$ for a given ionization laser intensity.

III. EXPERIMENTAL RESULTS

Figure 1 shows representative measurements of $Y(t)$ for OCS^+ at 45, 70, and 200 TW/cm^2 [Figs. 1(a)–1(c), respectively] and OCS^{2+} at 200 TW/cm^2 [Fig. 1(d)]. The alignment pulse parameters were held approximately constant for all data sets, and no significant dissociative ionization was observed at the two lowest ionization intensities. At the highest ionization intensity, the amount of dissociative ionization is difficult to quantify precisely, but its addition to the OCS^+ parent ion yield results in an angle dependence of the net OCS^+ yield that is similar to that of the parent cation alone. Inclusion of dissociative ionization channels in the OCS^{2+} yield has a greater influence, noticeably reducing the anisotropy on the angular distribution (see Sec. IV B). Clear variations in the normalized ionization yield are observed at delays near the half- and full-rotational revival times, 41 and 82 ps, due to the substantial changes in the molecular angular distribution (from preferentially parallel to preferentially perpendicular with respect to the ionizing laser polarization) near those delays. The modulations are largest for OCS^{2+} and they are nearly identical for the two lower-intensity OCS^+ data sets. The relatively small variations in $Y(t)$ for the high-intensity OCS^+ data are due to saturation of the ionization probability at unity, independent of the molecular alignment.

Although not apparent in Fig. 1, the data consistently show that $Y(t)$ is ∼2–3 % greater than unity for $t < 0$ where the alignment pulse follows the ionization pulse. That is, the ionization signal with the alignment pulse appearing second is slightly larger than with the ionization pulse alone. This suggests that even though the alignment pulse produces no significant ionization on its own, it may ionize a small amount of electronically excited population produced by an ionization pulse preceding it. While not entirely surprising, this small effect has some bearing on our data analysis as described in more detail in Sec. IV A.

Figure 2 shows the unaligned OCS^+ and OCS^{2+} ionization yields as a function of laser intensity. At the lowest intensity, the singly and doubly charged ion yields increase rapidly with increasing laser intensity, as expected for tunneling or high-order multiphoton ionization. At the highest intensity, the OCS^+ and OCS^{2+} ion yields are fully saturated, are comparable in magnitude, and are essentially independent of laser intensity.

Following Hankin *et al.* [62], we separately fit the high- and low-intensity portions of the measured yields to curves of the form αI^β, where I is the peak intensity of the ionization pulse. We then define a saturation intensity as the point of intersection of the two curves which take the form of straight

lines on a log-log plot of yield vs intensity, such as that shown in Fig. 2. For OCS^+ the data in Fig. 1 were collected below, near, and above the OCS saturation intensity $I_{OCS} \simeq 70$ TW/cm^2. The strong similarity of the measured $Y(t)$ curves in Figs. 1(a) and 1(b) indicates that the angle dependence of the strong-field ionization rate is essentially independent of intensity below I_{OCS}. Due to the high ionization rate well above I_{OCS}, the ionization probability is near unity regardless of the molecular alignment angle, resulting in depletion saturated yields with relatively small variations in $Y(t)$ as observed in Fig. 1(c).

The peak ionization laser intensity is calibrated by measuring the ionization yields for background N_2 and O_2 gas in the vacuum chamber, as a function of laser pulse energy, and employing the same αI^β fit, above and below saturation, as described above. Empirically, we find that similarly determined saturation intensities reported for noble-gas atoms [62] correspond to the intensities at which Ammosov-Delone-Krainov (ADK) theory predicts 15% ionization for those atoms. We use this observation, along with previous measurements of ionization rate ratios for N_2:Ar and O_2:Xe [63,64], to predict saturation intensities for N_2 and O_2 from ADK calculations for Ar and Xe. Scaling the experimental intensity so that the measured and predicted saturation intensities agree, we consistently obtain very good agreement with previous measurements of the intensity-dependent ionization yields for both N_2 and O_2 [65]. This intensity calibration is used, without any additional rescaling, to directly compare the measured and calculated angle-dependent ionization yields for OCS^+ and OCS^{2+}.

IV. ANALYSIS: EXTRACTING ANGLE DEPENDENCE FROM DELAY-DEPENDENT IONIZATION YIELDS

For a (nearly) rigid linear molecule like OCS, symmetry dictates that the ionization probability depends only on the angle θ between the laser polarization and the molecular axis. Given the relatively large focal diameter of our alignment beam relative to the ionization beam, the angular probability distribution is nearly identical for all molecules in the ionization volume and the delay-dependent ionization yield can be written

$$Y(t) = \int_0^\pi \Upsilon(\theta) S(\theta, t) \sin(\theta) d\theta, \tag{1}$$

where $S(\theta, t)$ is the delay-dependent ensemble average of the angular probability distribution (in other words, it is the angular probability distribution for an "average" molecule) and $\Upsilon(\theta)$ is the angle-dependent molecular ionization yield which we wish to extract from measurements of $Y(t)$. The yield $\Upsilon(\theta)$ is not strictly equal to the angle-dependent strong-field ionization probability $P(\theta)$, since the former depends on the spatial intensity distribution of the ionizing laser near its focus. However, due to the nonlinear dependence of $P(\theta)$ below the saturation intensity, the dominant contribution to $\Upsilon(\theta)$ comes from very near the center of the focal volume where the highest ionization intensity is produced. In this case, $P(\theta) \propto \Upsilon(\theta)$ at the maximum intensity in the ionizing laser focus. Well above saturation, however, a non-negligible contribution to $\Upsilon(\theta)$ can come from a larger volume surrounding the focus, so $\Upsilon(\theta)$ is not simply proportional to $P(\theta)$ at the maximum ionization intensity. Our use of a narrow molecular beam reduces this volume averaging effect, but does not eliminate it [66]. Rather than attempt to accurately model the spatial intensity distribution at the laser focus and extract $P(\theta)$ from $\Upsilon(\theta)$ by deconvolution, we approximate $P(\theta) \propto \Upsilon(\theta)$, as is the case at low intensity. As shown in Sec. IV B, despite this approximation we find good agreement between experimental determinations of $\Upsilon(\theta)$ and calculated distributions $P(\theta)$ even at ionization intensities $I > I_{OCS}$.

To extract $\Upsilon(\theta)$ from measurements of $Y(t)$, we take advantage of the fact that $S(\theta, t)$ can be calculated with high accuracy for a thermal ensemble of (nearly) rigid molecular rotors with rotational temperature T subjected to an alignment pulse with a known time-dependent intensity [10,19,56]. Assuming $S(\theta, t)$ is known, one can write $\Upsilon(\theta)$ in terms of a complete set of real functions $f_k(\theta)$,

$$\Upsilon(\theta) = \sum_k a_k f_k(\theta), \tag{2}$$

where the a_k are real coefficients. With this expansion one can express $Y(t)$ as

$$Y(t) = \sum_k a_k M_k(t), \tag{3}$$

where $M_k(t)$ is a moment of $S(\theta, t)$ with respect to the expansion function $f_k(\theta)$,

$$M_k(t) = \int_0^\pi f_k(\theta) S(\theta, t) \sin(\theta) d\theta. \tag{4}$$

The $M_k(t)$ can be readily calculated if $S(\theta, t)$ is known, allowing one to fit measurements of $Y(t)$ to obtain the expansion coefficients a_k and enabling the reconstruction of $\Upsilon(\theta)$. Following this approach, the angular resolution in the determination of $\Upsilon(\theta)$ is not limited by the degree of alignment of the molecular ensemble. Instead, it depends on the highest spatial frequencies present in the statistically relevant basis functions required for the fit and therefore is limited by the signal-to-noise ratio in the measurements of $Y(t)$. As discussed in more detail below, with the appropriate choice of basis functions, only two or three nonzero coefficients are required within our signal-to-noise ratio to obtain a $\Upsilon(\theta)$ distribution for single ionization of OCS which is in very good agreement with previous measurements.

Calculating $S(\theta, t)$ involves numerical integration of the time-dependent Schrödinger equation [10], requiring input of the established rotational constant $B_{OCS} \simeq 0.2028$ cm^{-1} and anisotropic polarizability $\Delta\alpha_{OCS} \simeq 31$ a.u. [67,68], the temporal intensity profile of the alignment laser, and the initial rotational temperature T of the thermal ensemble. Based on FROG measurements [61], our alignment laser pulse is known to have a near Gaussian temporal profile with a full width at half maximum of 75 fs. Rather than rely on estimates of the peak alignment laser intensity at the focus I_0 and T, we allow these parameters to vary along with the expansion coefficients a_k to obtain the best overall fit to $Y(t)$. The recovered values for I_0 and T are in reasonable agreement with those estimated from measured laser beam properties and from previous performance characteristics of the Even-Lavie valve, respectively.

A. Fitting procedure

Given our experimental conditions, the OCS molecules in our sample can be aligned, but not oriented, along the laser polarization axis. Accordingly, we have $\Upsilon(\theta) = \Upsilon(\pi - \theta) \geqslant 0$ for $0 \leqslant \theta \leqslant \pi$. Rather than attempt to construct $\Upsilon(\theta)$ from a complete orthonormal basis, we choose functions that individually satisfy the constraints noted above, each serving to allow for structure with a simple n-fold symmetry. Because the $Y(t)$ measurements indicate a minimum in the ionization probability for molecules preferentially aligned along the laser polarization [based on comparisons with the calculated time dependence of $\langle\cos^2(\theta)\rangle(t)$], we select basis functions with this same property. Specifically, we write

$$\Upsilon(\theta) = a_0 + a_1 \sin^2(\theta) + a_2 \sin^2(2\theta) + a_3 \sin^2(3\theta) + \cdots . \tag{5}$$

Because rapid angular variations in $\Upsilon(\theta)$ are unlikely, this approach allows us to produce structures that are physically realistic while requiring relatively few basis functions for a good fit. We do not restrict the a_k to positive values so, in principle, contributions from the different terms can interfere. However, in practice, we find that the non-negligible coefficients from the optimum fits are always positive.

To perform the fits, $S(\theta, t)$ is first calculated on a grid of (T, I_0) pairs and the best coefficients a_k are determined at each grid point using a least-squares fit, comparing the calculated and measured values of $Y(t)$ for delays $t > 0$. By restricting the fitting to $t > 0$, we avoid the large enhancement in the ionization signal at delays where the alignment and ionization pulses overlap in time. We do however normalize the a_k coefficients by insisting that the calculated value of $Y(t) = 1$ for $t < 0$, since in that case the alignment pulse follows the ionizing pulse, and our model neglects the possibility of electronic excitation by either one. This approach yields a reasonable estimate for T and I_0 as well as the a_k. Furthermore, plotting the χ^2 (or its reduced counterpart χ^2_ν, both being a figure of merit for the fitting procedure [69]) provides an estimate of the temperature and intensity ranges that can result in a reasonable fit. Figure 3 shows such a plot, obtained using three basis functions for the fitting (using two or four terms gives qualitatively similar results). As shown in Fig. 3, the (reduced) χ^2 typically exhibits a pronounced minimum enabling a robust determination of both T and I_0.

To determine the maximum number of terms needed to achieve the best statistically relevant fit, we perform the F-test [69,70]. This test compares two fits carried out with the same values of T and I_0, one fit performed with k basis functions and the other with $k + 1$. The F-test gives the probability that any improvement in the fit with $k + 1$ terms is due solely to chance and not because it is a better description of the data. If the test probability is higher than a threshold value (we choose 5%), adding the extra term is not warranted. By performing the F-test for each intensity-temperature pair, we find that for OCS^+ only three basis functions [1, $\sin^2(\theta)$, and $\sin^2(2\theta)$] are warranted independent of I. In the case of OCS^{2+}, only the first two terms are included, since the third is found to be consistent with zero.

The final determination of $\Upsilon(\theta)$ through the best fit to $Y(t)$ is accomplished with a simplex search algorithm implemented in MATLAB [71]. Here T, I_0, and a_k coefficients, and two additional parameters were varied to minimize χ^2. The first of these two parameters allows for a slight rescaling of the relative yields. We find that the quality of the fits, primarily in the flat regions in $Y(t)$ between revival structures (see Fig. 1), is notably improved by allowing the imposed normalization at $Y(t < 0)$ to differ slightly (in all cases less than 1%) from unity. While the recovered form of $\Upsilon(\theta)$ is similar with or without this extra degree of freedom in the fits, the improvement in χ^2 through its inclusion is significant, presumably because it allows us to take into account small contributions from electronic excitation within the alignment pulse that is not included in our basic alignment model. The apparent impact on the data of electronic excitation within the ionizing pulse and subsequent ionization by the alignment pulse for $t < 0$ was already discussed in Sec. III. The second additional parameter allows for a slight rescaling of the recorded time delay by about 0.5%. This correction is required to accurately fit the yield variations at both the half- and full-revival times and is warranted because the actuator used to control the delay between the alignment and ionization pulses (Thorlabs Z825B) has a limited relative accuracy which is consistent with this rescaling. Finally, we note that the zero delay point is absolutely identified by measuring the enhanced ionization signal of the overlapping pulses with high temporal resolution. No additional delay offset parameter is needed for the fits.

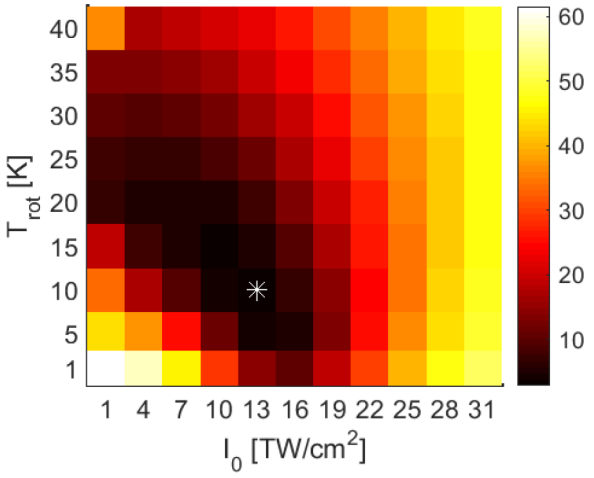

FIG. 3. Map of χ^2_ν as a function of rotational temperature T and alignment laser intensity I_0 for a typical data set. The white asterisk marks the point ($I_0 = 13$ TW/cm^2, $T = 10$ K) which gives the best agreement between data and the fit with $\chi^2_\nu = 2.87$.

B. Angle-dependent yields

Figure 4 shows the average $\Upsilon(\theta)$ determinations, resulting from fits to multiple measurements of $Y(t)$ analogous to those shown in Fig. 1, and described by the fitting parameters provided in Table I. For a given ionization intensity the fitting procedure was performed on each individual $Y(t)$ data set, obtaining a set of coefficients $\{a_0, a_1, a_2\}_I$, and the mean and the standard deviation for each coefficient were calculated (see Table I). For ease of comparison at different ionization intensities, we separately normalize $\Upsilon(\theta)$ at each intensity such that $\int_0^\pi \Upsilon(\theta)\sin(\theta)d\theta = 1$. In Fig. 4 we visualize the

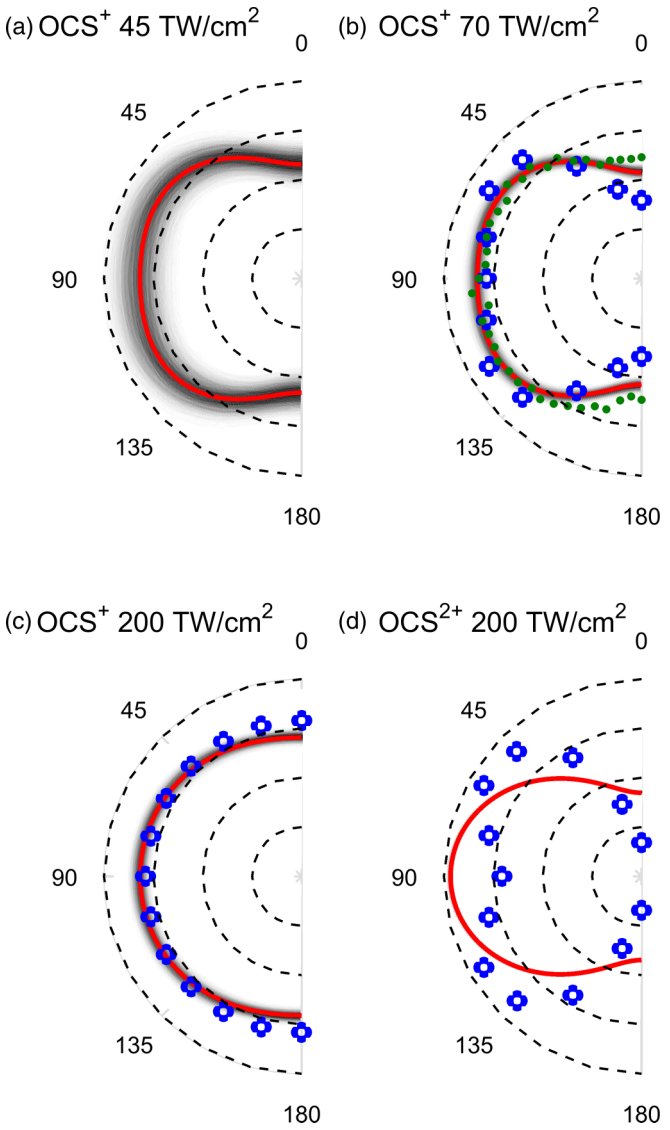

FIG. 4. Angular dependence of the ionization yield. Each red curve shows the average of the best fits to multiple measurements of the normalized time-dependent yields $Y(t)$. Blue flowers in (b)–(d) are the results of TDDFT calculations as described in Sec. V A. The small solid green circles in (b) are the experimental results from Hansen *et al.* [13] obtained with 30-fs pulses at 150 TW/cm^2. The grayscale shading illustrates the experimental uncertainty distribution associated with the standard deviation of the coefficients a_k obtained from averaging the relevant data sets.

uncertainty in the yield at each angle using a grayscale shading in the radial direction. The shading is determined by generating a large set of angular dependences, in a Monte Carlo fashion, using coefficients whose values are randomly varied about their best-fit values, according to Gaussian probability distributions determined by the uncertainties in the respective coefficients. The grayscale shows the resulting distribution of the Monte Carlo results. As expected, $\Upsilon(\theta)$ for the OCS^+ parent at 200 TW/cm^2 is nearly isotropic since the single-ionization probability is saturated at that intensity. The deviation from perfect isotropy would be reduced somewhat if the contribution of $OC + S^+$ dissociative channels to the total single-ionization yield were included. The branching ratio into this channel is relatively low, but is hard to precisely quantify in our apparatus due to the overlap of S^+ with $O_2{}^+$ ions from small numbers of contaminant O_2 molecules. Below the saturation intensity, however, the OCS ionization has a minimum when the ionizing laser is polarized parallel to the molecular axis. Moreover, as shown in Figs. 4(a) and 4(b) and in Table I, $\Upsilon(\theta)$ is essentially independent of ionization intensity for $I \leqslant I_{\mathrm{OCS}}$. As Table I explicitly shows, at low intensities there is a significant contribution from the quadrupolelike basis function $\sin^2(2\theta)$, which is responsible for a small enhancement of the yield near 45° and 135°. This angular dependence is perhaps not surprising considering the shape of the highest occupied molecular orbital (HOMO), which has a strong quadrupole character [72].

Our results below saturation are consistent with previous findings [13]. In particular, Fig. 4(b) shows good agreement between our results and the measurements of Hansen *et al.* [13] for which the molecular angular distributions were explicitly measured rather than inferred from fits. This agreement provides an important benchmark of the effectiveness of our approach. It is worth noting that the data from Hansen *et al.* were collected at a somewhat higher intensity (150 TW/cm^2), but with a shorter pulse duration (30 fs). Given the shorter ionization window and (small) uncertainties in the intensity calibrations for the respective measurements, it seems likely that the data of Hansen *et al.* were also collected near or below the intensity where significant saturation plays a role. An ionization intensity somewhat higher than ours is consistent with the slightly reduced contrast between the measured yields at 0° and 90° from Hansen *et al.*, as compared to ours.

In contrast to the single-ionization case, the strong dipole character observed for the doubly charged ion yield is remarkable, with no apparent quadrupolelike component. The inclusion of a weak dissociative ionization channel, likely $O^+ + CS^+$, which is also dipolar but with yield maxima at 0° and 180°, somewhat reduces the anisotropy observed in the parent dication alone. In the following sections we compare our experimental results with those of TDDFT calculations. In addition, we analyze the calculated time-dependent one-body

TABLE I. Estimated coefficients a_k (mean and standard deviation) in the best-fit expansion of $\Upsilon(\theta)$ obtained from fits to $Y(t)$ from multiple data runs at different ionization laser intensities and for different charge states.

Ionic species, intensity	a_0	a_1	a_2	No. of data sets averaged
OCS^+, 45 TW/cm^2	2.31 ± 0.19	0.96 ± 0.2	0.36 ± 0.1	2
OCS^+, 70 TW/cm^2	2.15 ± 0.07	1.17 ± 0.07	0.39 ± 0.05	3
OCS^+, 200 TW/cm^2	2.82 ± 0.07	0.45 ± 0.06	0.05 ± 0.05	2
OCS^{2+}, 200 TW/cm^2	1.7 ± 0.016	2.17 ± 0.023		2

density to shed light on the localization of the hole on the target following strong-field ionization.

V. THEORETICAL APPROACH

Our TDDFT treatment of strong-field ionization in OCS is based on the work of Sissay *et al.* [41]. Briefly, the one-body density is propagated using an atomic orbital basis of Gaussian functions. We use the aug-cc-pVTZ basis set [73] on each atom, augmented with an additional Schlegel medium absorbing basis [43,74]. The OCS geometry was obtained by optimizing with the PBE0 functional [75], which is a hybrid built from the PBE (Perdew, Burke, and Ernzerhof) functional [76] with a 25% admixture of Hartree-Fock exchange. For ionization calculations we use the LC-PBE0* range-separated function [77–80], tuned such that the first ionization potential as determined from a self-consistent field computation is consistent with the HOMO eigenvalue (i.e., Koopman's theorem is satisfied). This resulted in a range separation parameter of $\gamma = 0.409$ a.u.$^{-1}$ (inverse length) and a first ionization potential of 11.4 eV (experimental value 11.2 eV). Tuned range-separated functionals like this have decreased self-interaction errors, the correct asymptotic form of the Coulomb potential, and improved ionization energies for orbitals. In the context of alignment and intensity-dependent yields or rates, these have been shown to improve the accuracy of TDDFT computations [41]. Finally, due to the dependence of the potential on the time-dependent (polarized) density, all-electron TDDFT simulations naturally include both field dressing and multiorbital (channel) ionization effects, the accuracy of which is dictated by the functional.

To mimic outgoing flux, we use a complex absorbing potential (CAP) positioned on each atom. This results in a small overlap between the CAPs and the occupied field-free molecular orbitals, leading to a spurious leakage of electrons irrespective of the laser field parameters. The position of the CAPs is optimized to find a balance between such undesirable self-ionization (too close) and insufficient overlap with the atom-centered basis functions resulting in missing ionization events (too far). In practice, the CAP position was optimized by choosing a position where the ionization yield (or rate) is insensitive to the chosen position. For details we refer to [41]. This resulted in a CAP with a sine-squared shape starting 6.0 Å from each atom and extending over 10 Å. Computed yields were then corrected for an estimate of the leakage contribution, defined as the charge loss for a simulation of the same duration but without any field. This estimated leakage was obtained by extrapolating the instantaneous charge loss over the first few laser cycles (when the field is too weak to induce any "real" ionization and therefore all electron losses are due to spurious leakage) to the end of the pulse. Irrespective of the intensity and angle, for all data shown here we find the leakage rate approximately equal to 1.983×10^{-3} electrons/a.u.. Despite this correction, and because of the exponential dependence of ionization on the peak intensity, we are limited in practice to a range of intensities where the yield is at least comparable to that of the leakage, here a few percent over the 37-fs duration of the pulse.

A. Single- and double-ionization yields

To match the experimental parameters as closely as possible, we compute ionization yields using a 800-nm laser pulse that has a sine-square envelope with 37-fs FWHM in intensity duration. In practice, computations were run a little longer after the end of the pulse (106 fs total) to allow for any residual ionized electron flux near the core to reach the CAPs. The ionization yields are directly related to the number of electrons left in the simulation domain at the end of the pulse. Since OCS targets are perfectly oriented in TDDFT computations while the experiments only achieve alignment, the yields reported in Fig. 4 have been averaged over supplementary angles (θ and $\pi - \theta$). We note, though, that because of the up-down field symmetry and long duration of the laser pulses considered here, up- and down-oriented molecules experience close to identical conditions and, as expected, we find that the oriented yields are virtually identical to their supplementary angle-averaged counterparts.

Although we are interested in both single- and double-ionization yields, there is no known density functional that separates these quantities for use with the TDDFT one-body density. Instead, we focus on the low- and high-intensity regimes where one or the other of the contributions (single or double ionization) can be neglected. Obviously, a shortcoming of our density-based ionization model is the inability to disentangle the single- and double-ionization signals at intermediate intensities, where the single-ionization yield is not yet saturated or where saturation exists only for some alignment angles. In practice, for the pulse durations we consider here, we reliably compute single-ionization signals in a range of about 60–150 TW/cm^2. The upper bound corresponds to the intensity around which neutral depletion washes out any angular dependence in the yield. The lower bound is determined by the electron leakage described above, explaining the lack of TDDFT results in Fig. 4(a). This lower bound also means that we cannot accurately model the ionization yield throughout the laser focus and thus prevents us from making a direct comparison between calculated and measured yields shown in Fig. 2. Instead, as described in Sec. III, we define the saturation intensity for single and double ionization as that which produces an angle-integrated ionization probability of 15%. Numerically we find 70 TW/cm^2 for the single- and 180 TW/cm^2 for the double-ionization saturation intensities, respectively. These values are in excellent and reasonable agreement with the corresponding experimental determinations of 70 and 240 TW/cm^2, respectively.

At the lowest intensities, the single-ionization yield corresponds directly to the amount of charge lost at the end of the computation (after leakage correction; see above), because we can safely ignore double ionization, in agreement with experimental measurements (see Fig. 2). The result is displayed in Fig. 4(b) and shows very good agreement with experimental measurements. The angle-resolved yield matches the experimentally observed peanut shape with maximum ionization at perpendicular alignment and minimum at parallel alignment. Overall, the larger perpendicular ionization rate loosely matches the shape of the HOMO, but our results provide a significant improvement over previous MOADK calculations which instead predict a cloverleaf shape with a strong minimum at both 0° and 90° [13]. We attribute this difference

to multichannel ionization mechanism(s), which the full *ab initio* TDDFT computation is better equipped than MOADK calculations to capture. This multichannel mechanism is further revealed by the localization of a hole on the sulfur atom following strong-field ionization (see Sec. V B).

In the high-intensity limit, where the experimental single-ionization signal is saturated, we employ a simple model for calculating the angle-dependent double-ionization yields. We exploit the fact that at high intensities where non-negligible double ionization occurs, the single-ionization probability is isotropic [see Fig. 4(c)]. In other words, we assume that, irrespective of the angle, the target undergoes a full single ionization and any excess charge loss beyond that is attributed to double ionization. The results of the model calculation are displayed in Fig. 4(d). Apparently, this simple model does not qualitatively reproduce the experimental observations. We also tried an alternative model in which the single-ionization yield remains slightly anisotropic (as in the experiments) but no significant improvement was observed. Building on the success of single-ionization simulations, we also tried computing double ionization directly out of OCS^+, where the first electron was removed "by hand." We tried a relaxed and an unrelaxed nuclear structure and various orbital- or spin configurations for the initial hole. None of these succeeded in qualitatively reproducing the experimental peanut shape in Fig. 4(d).

The discrepancy between the experimental and TDDFT results can be attributed to one or more of the following. First and most fundamentally, there is, as mentioned above, the lack of a density functional that separates single and double ionization. Next, the model we have employed for high intensities [to explain Fig. 4(d)] assumes sequential double ionization, which may not be entirely valid. Assuming that sequential ionization is valid, it may be that double ionization reveals a level of inaccuracy in the long-range-corrected–PBE0* functional, due to the local-in-time adiabatic approximation [81,82] as well as incorrect orbital energies. Extending TDDFT to the treatment of multiple ionization is an area of ongoing work; see, for example, the orbital-based (rather than density-based) approaches in [83,84]. Regardless, our experimental angle-dependent double-ionization results serve as a benchmark for improvements in strong-field ionization theory.

B. Two-center ionization model

Building on the good agreement of TDDFT single-ionization yields with experiment, in this section we aim at gaining further insight into the time-dependent ionization dynamics. In particular, we want to understand how ionization unfolds at the subcycle level and how the orientation of the molecule influences the cation state that is formed. Here we assign time-dependent charges to each atom using the Bader method [57–60], which defines a self-consistent partitioning of the one-body electron density around each atom, or group of atoms, and therefore an effective charge. A chemically relevant and meaningful definition of such partitioning and partial charges can be a challenging task for complex molecules and is, on its own, an active field of research, most often performed on the ground-state density. In contrast, the relative simplicity of our model, in which the OCS molecule is reduced to two centers (carbon and oxygen are grouped together), allows us to employ the Bader partitioning method to the time-dependent electron density and we follow the effective number of electrons on the S and CO centers as the system is driven by the laser. An illustration of Bader charge partitioning of ground-state OCS is displayed in Fig. 5.

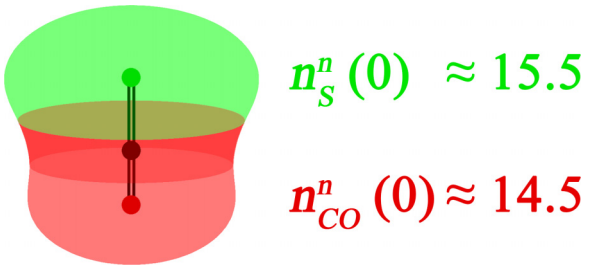

FIG. 5. Illustration of the Bader method and reduced two-center representation on ground-state OCS. The TDDFT one-body density is decomposed into three components (different shades on the left), each associated with one of the atomic centers. After grouping the C and O, we obtain an effective number of electrons on the two ends of the molecule. Compared to their atomic charges, 6+8 for CO and 16 for S, the observed excess and deficit of charge on the two ends, respectively, are consistent with their relative electronegativity (larger for O).

Although we are most interested in the OCS^+ electronic structure following ionization, that information is obscured in the Bader charge numbers by effects associated with the neutral density and the polarizability of the molecule. Thus, in what follows, we first carefully identify and then remove these effects to reveal the hole localization after strong-field ionization. Figures 6(a) and 6(b) shows the time-dependent charge on the two centers for a laser-driven target (solid curves) for a constant intensity envelope field with six-laser-cycle ramp-up. Even at low intensity, where there is no ionization, the neutral OCS density is reshaped by external electric fields, which translates to a rearrangement of the Bader partial charges observed on each effective center. Note that the curves in Figs. 6(a) and 6(b) oscillate out of phase. While any electric field is expected to induce a distortion of the one-body electron density, here we are more interested in displacement of electron(s) from one region in the molecule to another. At the leading order, a component of the electric field only displaces density along its direction. Such a rearrangement is mediated by the molecular bonds and therefore in leading order we expect that charge displacement will be associated with the component of the electric field parallel to the molecular axis $E_\parallel$. Additionally, we only consider the linear response in the field.[1] These hypotheses are confirmed below by our overall numerical analysis and results. To this end, we first define the

[1]In general, partial atomic charges may depend on higher-order terms in the field. In our case, however, we observed a linear dependence on $E_\parallel$. Based on this, we build our model assuming a linear response and validate in two ways: error bars from varying the fit windows and angle dependence (equivalent to varying the magnitude of $E_\parallel$). This analysis could be generalized to the cases where the response is nonlinear in the field, provided one can meaningfully isolate the ion signal.

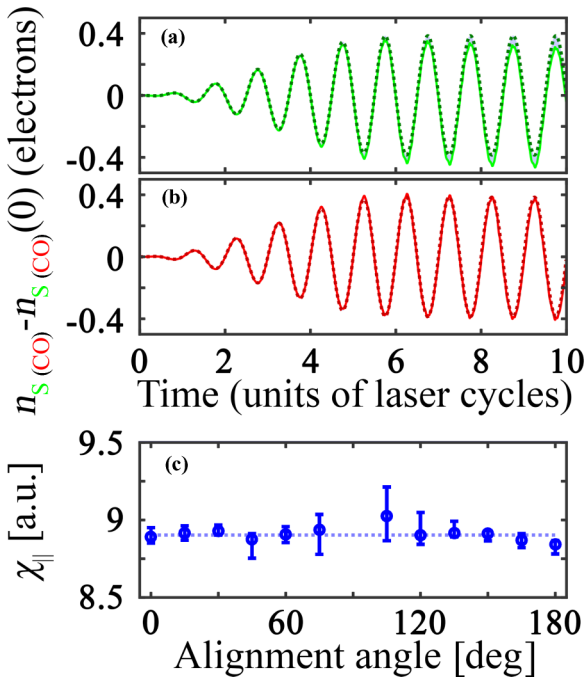

FIG. 6. Illustration of the time-dependent Bader charge on the (a) S and (b) CO centers (solid curves) for a constant intensity envelope field with six-laser-cycle ramp-up, 70-TW/cm^2 peak intensity, 800-nm wavelength, and 15° alignment angle with the molecular axis. For clarity we show the fluctuation around the field-free values. The dotted curves correspond to the neutral-only signal with generalized-atomic-susceptibility effects of Eq. (6) and fitted from the beginning of the ramp-up. (c) Reconstructed generalized atomic susceptibility for different alignment angles. Error bars correspond to extrema solutions when varying the fit window. At 90°, where $E_\parallel$ vanishes, the generalized susceptibility of Eq. (6) is ill-defined and has been excluded from the plot.

generalized atomic susceptibility $\chi_\parallel$,

$$\begin{aligned} n^n_{\rm S}(t) &= n^n_{\rm S}(0) - \chi_\parallel E_\parallel(t), \\ n^n_{\rm CO}(t) &= n^n_{\rm CO}(0) + \chi_\parallel E_\parallel(t), \end{aligned} \tag{6}$$

where $n^n_{\rm S\,(CO)}$ is the effective number of electrons on the (neutral) S (CO) center and $t = 0$ corresponds to the field-free case. Note that the equations fulfill charge conservation $n^n_{\rm S} + n^n_{\rm CO} = 30$ at all times. In essence, the generalized atomic susceptibility represents the ease with which an electric field polarizes the electron density around a particular atom. This allows us to disentangle ionization effects from less interesting transient polarization.

In practice, the generalized atomic susceptibility is computed from the Bader charges at the beginning of the laser pulse, when the field is ramping up and before it is strong enough to induce any ionization. We use a least-squares fit to Eq. (6) to find $\chi_\parallel$,

$$\begin{aligned} \chi_\parallel = \underset{\alpha}{\rm argmin} \int_0^\tau & \left[n_{\rm S}(t) - n^n_{\rm S}(0) + \alpha E_\parallel(t)\right]^2 \\ & + \left[n_{\rm CO}(t) - n^n_{\rm CO}(0) - \alpha E_\parallel(t)\right]^2 dt. \end{aligned} \tag{7}$$

Here τ is the window over which the fit is performed and argmin is the argument of the minimum [i.e., $\chi_\parallel$ is the value of α where the minimum is obtained in Eq. (7)]. In the computations shown in Fig. 6(c), we scan the fit window between $\tau = 2.5$ and $\tau = 3.5$ laser cycles. As explained above, the upper bound was chosen such as to ensure that no ionization contaminates the neutral susceptibility value and the lower bound was chosen to assess the robustness of the fit. We select the average value obtained from scanning the fit window as the generalized atomic susceptibility, while extrema define the error bars. The generalized atomic susceptibility is found to be practically independent of molecular alignment. This further supports our two-center interpretation of the laser-driven OCS charge dynamics. Note that our analysis does not require the susceptibility to be independent of the alignment angle. For targets more complicated than small linear molecules, we generally expect it not to be so. Here we take advantage of this property of OCS as an independent check for our model and following analysis.

At peak field intensity, i.e., when the laser does ionize the target, the TDDFT one-body density corresponds to a superposition of neutral and cation components. In other words, the deviation between the actual partial charge $n_{\rm S\,(CO)}(t)$ and extrapolation of the neutral-only $n_{\rm S\,(CO)}(0) \mp \chi_\parallel E_\parallel(t)$ signals reveals the OCS$^+$ instantaneous electronic structure. More specifically, we can define this difference as the electron hole number on each center

$$\begin{aligned} \Delta n^c_{\rm S}(t) &= n^n_{\rm S}(0) - \chi_\parallel E_\parallel(t) - n_{\rm S}(t), \\ \Delta n^c_{\rm CO}(t) &= n^n_{\rm CO}(0) + \chi_\parallel E_\parallel(t) - n_{\rm CO}(t). \end{aligned} \tag{8}$$

One can see that we have defined the susceptibility so as to minimize the electron hole number on each center in the absence of ionization. For technical reasons associated with our implementation of the Bader charge method,[2] the hole numbers computed with the equations above are noisy. In Fig. 7(a) we show a smoothed version of the signal (solid curves), obtained by convolution with a Gaussian kernel with 1/20 of a laser cycle standard deviation. Similar to the neutral component, the partial charge on the two cation centers is strongly modulated by the laser and is responsible for the large out-of-phase oscillations in Fig. 7(a). These oscillations, together with the numerical noise, cancel out in the total hole number $\Delta n^c_{\rm tot} = \Delta n^c_{\rm S} + \Delta n^c_{\rm CO}$. The remaining staircase shape in the total hole number reflects the subcycle ionization dynamics, i.e., alternating fast and slow increasing total hole number following extrema and zeros of the field.

Unlike the neutral component, the partial hole numbers do not allow us to define a generalized atomic susceptibility for

[2]As explained in Sec. V, TDDFT computations are performed on a (Gaussian) basis. For the Bader charge analysis, the resulting one-body density is then projected onto a grid. Because some of the core electrons, which do not participate in the hole dynamics of interest here, are very localized in space, they generate artifacts in the grid representation of the density (undersampling). While in theory such artifacts can be eliminated by reducing the grid spacing, in practice we find the computational and memory cost to do so prohibitive. Overall, the success of our cycle-average hole localization makes us confident in the relevance of our results, despite that noise.

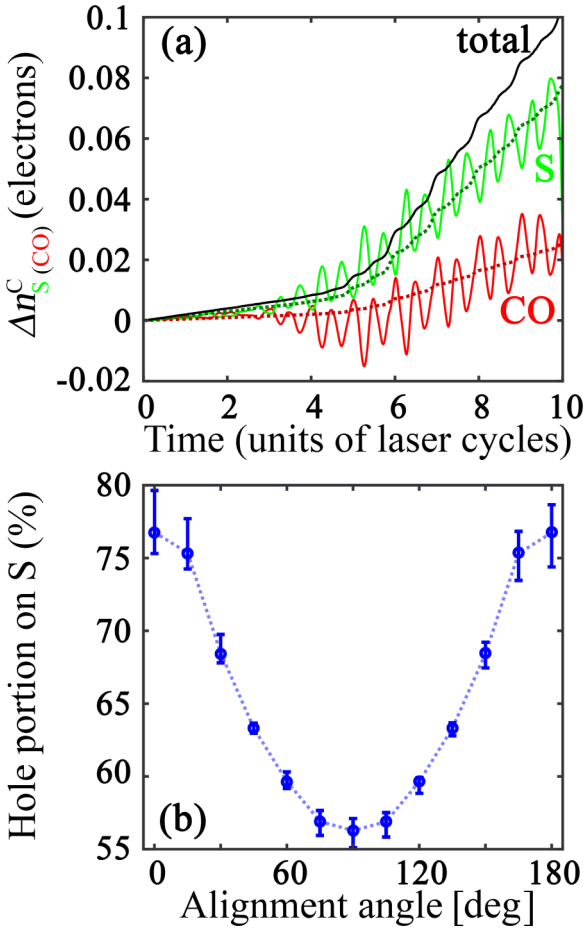

FIG. 7. (a) Smoothed hole number on the S and CO centers (solid curves), associated with Eq. (8), and the total hole number (no smoothing applied) for the same laser parameters as in Fig. 6. The dashed curves represent the cycle-averaged portion of hole on each center. (b) Reconstructed cycle-averaged portion of electron hole on the cation S center as a function of the alignment angle. Error bars correspond to extrema solutions when varying the fit window.

OCS^+. Instead, they allow us to determine the cycle-averaged localization of the hole on either of the centers. For instance, the cycle-averaged portion of the hole found on the S end, α_S, is defined as

$$\alpha_S = \underset{\alpha}{\operatorname{argmin}} \int_{\tau}^{\tau+\Delta\tau} \left[\Delta n^c_S(t) - \alpha \Delta n^c_{\rm tot}(t)\right]^2 + \left[\Delta n^c_{CO}(t) - (1-\alpha)\Delta n^c_{\rm tot}(t)\right]^2 dt \quad (9)$$

where τ is some time during the constant intensity part of the laser pulse and the duration $\Delta\tau$ spans an integer number of laser cycles. As before, we define α_S in a least-squares sense as the value of α that minimizes Eq. (9). Then, because of charge conservation, the proportion on CO is simply $1-\alpha_S$. In practice, for the fits reported here, we take $\Delta\tau = 3$ laser cycles and τ spanning six to seven laser cycles (the first laser cycle immediately following the end of the ramp-up). Here as well, we select the average value of the fits over different windows as the portion of the hole residing on S while extrema define the error bars. In Fig. 7(a) we illustrate and compare the result of the fit [Eq. (9)] (dashed curves) with their underlying signals (solid curves). Note that, because of the cycle-averaged definition used in Eq. (9), the large oscillations in the full time-dependent signal are eliminated in the fit. The good agreement between the two sets of curves (dotted-solid pairs) supports the physical significance of our hole localization model and, as a consequence, our capability to infer the OCS^+ cation electronic structure following strong-field ionization.

In Fig. 7(b) we display the variation of the hole localization on the S center as the laser polarization direction is varied relative to the molecular axis. Clearly, it shows that hole localization on one end (S) of the molecule following strong-field ionization is strongly dependent upon alignment. This localized hole is a consequence of multichannel ionization. Indeed, only a combination of delocalized valence orbitals can result in a localized electron hole on one end of the molecule. We also note that the cycle-averaged hole is most localized, with about 3/4 on the S center, when the field and molecule are aligned. This may be due to the combined action of the molecular and laser potentials, resulting in greater selectivity as to where and when electrons can be removed from the target. On the other hand, with the field perpendicular to the molecular axis, both centers are able to contribute throughout the laser cycle, ultimately resulting in a more delocalized hole.

Our results clearly show that molecular alignment provides a way to control the dynamic cation electronic structure. This has important implications, e.g., in attosecond physics where subsequent migration of that hole, how to observe it and how to control it, is the subject of substantial current attention. These results suggest that molecular orientation or alignment can have a significant effect on electron dynamics following ionization. Indeed, a localized initial state is likely to be a necessary condition for attosecond charge migration. The generalization of our analysis to targets other than OCS will likely depend upon a balance between two competing features of the laser-driven electron density. On the one hand, the generalized atomic susceptibility should be large enough to be determined before the target undergoes ionization. On the other hand, the reconstructed hole number signal of Eq. (8) should be clean enough to yield meaningful information on the cation electronic structure following strong-field ionization. In the case of OCS, that balance leans more towards the former, with the result that, here, only the cycle-averaged hole localization on the two centers can be defined. Our results also suggest that strong-field ionization by on-axis light is more likely to initiate charge migration, despite having a lower yield than for molecules with a perpendicular orientation (see Fig. 4).

VI. SUMMARY

We have measured and calculated strong-field single- and double-ionization yields in OCS as a function of the angle between the molecular axis and the 800-nm laser polarization. For single ionization, the measured yields are in good agreement with previous measurements and with our TDDFT calculations, while differing substantially from previous calculations for ionization at 800 nm. Further analysis of the

electron density reveals, on average, over the laser cycle, the localization of the hole following strong-field ionization. We find that the hole is most localized on the S end with the laser polarization parallel to the molecular axis and delocalized over the molecule for perpendicular alignment. For double ionization, both experiment and theory show a minimum in the yield when the laser is aligned parallel to the ionizing laser. However, the sharper, dipolelike angular dependence observed in the experiments is not satisfactorily captured by the calculations. Indeed, extending TDDFT to accurately predict double-ionization yields is an ongoing challenge. The ability to accurately predict and understand angular-dependent strong-field ionization rates is critical for its employ as a trigger for fast electron motion within molecules and for controlling the ensuing correlated dynamics.

ACKNOWLEDGMENTS

The authors thank Henrik Stapelfeldt for numerous helpful discussions and for providing his group's angle-dependent strong-field single-ionization data for OCS. This work was supported by the U.S. Department of Energy, Office of Science, Basic Energy Sciences, under Award No. DE-SC0012462.

[1] K. J. Schafer, B. Yang, L. F. DiMauro, and K. C. Kulander, Phys. Rev. Lett. **70**, 1599 (1993).
[2] P. B. Corkum, Phys. Rev. Lett. **71**, 1994 (1993).
[3] P. B. Corkum and F. Krausz, Nat. Phys. **3**, 381 (2007).
[4] F. Krausz and M. Ivanov, Rev. Mod. Phys. **81**, 163 (2009).
[5] M. Meckel, D. Comtois, D. Zeidler, A. Staudte, D. Pavičić, D. H. C. Bandulet, H. Pépin, J. C. Kieffer, R. Dörner, D. M. Villeneuve, and P. B. Corkum, Science **320**, 1478 (2008).
[6] C. I. Blaga, J. Xu, A. D. DiChiara, E. Sistrunk, K. Zhang, P. Agostini, T. A. Miller, L. F. DiMauro, and C. D. Lin, Nature (London) **483**, 194 (2012).
[7] J. Xu, C. I. Blaga, K. Zhang, Y. H. Lai, C. D. Lin, T. A. Miller, P. Agostini, and L. F. DiMauro, Nat. Commun. **5**, 4635 (2014).
[8] X. M. Tong, Z. X. Zhao, and C. D. Lin, Phys. Rev. A **66**, 033402 (2002).
[9] I. V. Litvinyuk, K. F. Lee, P. W. Dooley, D. M. Rayner, D. M. Villeneuve, and P. B. Corkum, Phys. Rev. Lett. **90**, 233003 (2003).
[10] D. Pinkham and R. R. Jones, Phys. Rev. A **72**, 023418 (2005).
[11] D. Pavičić, K. F. Lee, D. M. Rayner, P. B. Corkum, and D. M. Villeneuve, Phys. Rev. Lett. **98**, 243001 (2007).
[12] E. Penka Fowe and A. D. Bandrauk, Phys. Rev. A **84**, 035402 (2011).
[13] J. L. Hansen, L. Holmegaard, J. H. Nielsen, H. Stapelfeldt, D. Dimitrovski, and L. B. Madsen, J. Phys. B **45**, 015101 (2012).
[14] E. Penka Fowe and A. D. Bandrauk, Can. J. Chem. **90**, 616 (2012).
[15] L. B. Madsen, F. Jensen, O. I. Tolstikhin, and T. Morishita, Phys. Rev. A **87**, 013406 (2013).
[16] A. Russakoff, S. Bubin, X. Xie, S. Erattupuzha, M. Kitzler, and K. Varga, Phys. Rev. A **91**, 023422 (2015).
[17] S. G. Walt, N. Bhargava Ram, A. von Conta, O. I. Tolstikhin, L. B. Madsen, F. Jensen, and H. J. Wörner, J. Phys. Chem. A **119**, 11772 (2015).
[18] R. Johansen, K. G. Bay, L. Christensen, J. Thøgersen, D. Dimitrovski, L. B. Madsen, and H. Stapelfeldt, J. Phys. B **49**, 205601 (2016).
[19] V. Makhija, X. Ren, D. Gockel, A.-T. Le, and V. Kumarappan, arXiv:1611.06476v2.
[20] M. Spanner and S. Patchkovskii, Phys. Rev. A **80**, 063411 (2009).
[21] Z. X. Zhao, X.-M. Tong, and C.-D. Lin, Phys. Rev. A **67**, 043404 (2003).
[22] S.-F. Zhao, C. Jin, A.-T. Le, T. F. Jiang, and C. D. Lin, Phys. Rev. A **80**, 051402 (2009).
[23] H. Li, D. Ray, S. De, I. Znakovskaya, W. Cao, G. Laurent, Z. Wang, M. F. Kling, A. T. Le, and C. L. Cocke, Phys. Rev. A **84**, 043429 (2011).
[24] V. H. Trinh, O. I. Tolstikhin, L. B. Madsen, and T. Morishita, Phys. Rev. A **87**, 043426 (2013).
[25] O. I. Tolstikhin, L. B. Madsen, and T. Morishita, Phys. Rev. A **89**, 013421 (2014).
[26] R. Saito, O. I Tolstikhin, L. B. Madsen, and T. Morishita, At. Data Nucl. Data Tables **103**, 4 (2015).
[27] K. C. Kulander, Phys. Rev. A **36**, 2726 (1987).
[28] L. A. A. Nikolopoulos, T. K. Kjeldsen, and L. B. Madsen, Phys. Rev. A **76**, 033402 (2007).
[29] B. Zhang, J. Yuan, and Z. Zhao, Phys. Rev. Lett. **111**, 163001 (2013).
[30] D. Bauer and F. Ceccherini, Opt. Express **8**, 377 (2001).
[31] X.- M. Tong and S.-I. Chu, Phys. Rev. A **64**, 013417 (2001).
[32] R. Baer, D. Neuhauser, P. R. Ždánská, and N. Moiseyev, Phys. Rev. A **68**, 043406 (2003).
[33] M. A. L. Marques and E. K. U. Gross, Annu. Rev. Phys. Chem. **55**, 427 (2004).
[34] S.-K. Son and S.-I. Chu, Phys. Rev. A **80**, 011403 (2009).
[35] D. A. Telnov and S.-I. Chu, Phys. Rev. A **79**, 041401 (2009).
[36] X. Chu, Phys. Rev. A **82**, 023407 (2010).
[37] X. Chu and M. McIntyre, Phys. Rev. A **83**, 013409 (2011).
[38] U. De Giovannini, D. Varsano, M. A. L. Marques, H. Appel, E. K. U. Gross, and A. Rubio, Phys. Rev. A **85**, 062515 (2012).
[39] M. Hellgren, E. Räsänen, and E. K. U. Gross, Phys. Rev. A **88**, 013414 (2013).
[40] A. Crawford-Uranga, U. De Giovannini, E. Räsänen, M. J. T. Oliveira, D. J. Mowbray, G. M. Nikolopoulos, E. T. Karamatskos, D. Markellos, P. Lambropoulos, S. Kurth, and A. Rubio, Phys. Rev. A **90**, 033412 (2014).
[41] A. Sissay, P. Abanador, F. Mauger, M. B. Gaarde, K. J. Schafer, and K. Lopata, J. Chem. Phys. **145**, 094105 (2016).
[42] A. Bruner, S. Hernandez, F. Mauger, P. M. Abanador, D. J. LaMaster, M. B. Gaarde, K. J. Schafer, and K. Lopata, J. Phys. Chem. Lett. **8**, 3991 (2017).
[43] P. Krause, J. A. Sonk, and H. B. Schlegel, J. Chem. Phys. **140**, 174113 (2014).
[44] P. Krause and H. B. Schlegel, J. Phys. Chem. Lett. **6**, 2140 (2015).

[45] P. Krause and H. B. Schlegel, J. Phys. Chem. A **119**, 10212 (2015).
[46] C.-L. Cheng, J. S. Evans, and T. V. Voorhis, Phys. Rev. B **74**, 155112 (2006).
[47] S. Meng and E. Kaxiras, J. Chem. Phys. **129**, 054110 (2008).
[48] T. Akama and H. Nakai, J. Chem. Phys. **132**, 054104 (2010).
[49] W. Liang, C. T. Chapman, and X. Li, J. Chem. Phys. **134**, 184102 (2011).
[50] K. Lopata and N. Govind, J. Chem. Theory Comput. **7**, 1344 (2011).
[51] K. Lopata and N. Govind, J. Chem. Theory Comput. **9**, 4939 (2013).
[52] R. G. Fernando, M. C. Balhoff, and K. Lopata, J. Chem. Theory Comput. **11**, 646 (2015).
[53] M. Valiev, E. J. Bylaska, N. Govind, K. Kowalski, T. P. Straatsma, H. J. J. Van Dam, D. Wang, J. Nieplocha, E. Apra, T. L. Windus, and W. A. de Jong, Comput. Phys. Commun. **181**, 1477 (2010).
[54] J. Mikosch, C. Z. Bisgaard, A. E. Boguslavskiy, I. Wilkinson, and A. Stolow, J. Chem. Phys. **139**, 024304 (2013).
[55] H. Stapelfeldt and T. Seideman, Rev. Mod. Phys. **75**, 543 (2003).
[56] C. Marceau, V. Makhija, D. Platzer, A. Yu. Naumov, P. B. Corkum, A. Stolow, D. M. Villeneuve, and P. Hockett, Phys. Rev. Lett. **119**, 083401 (2017).
[57] G. Henkelman, A. Arnaldsson, and H. Jónsson, Comput. Mater. Sci. **36**, 354 (2006).
[58] E. Sanville, S. D. Kenny, R. Smith, and G. Henkelman, J. Comput. Chem. **28**, 899 (2007).
[59] W. Tang, E. Sanville, and G. Henkelman, J. Phys.: Condens. Matter **21**, 084204 (2009).
[60] M. Yu and D. R. Trinkle, J. Chem. Phys. **134**, 064111 (2011).
[61] R. Trebino, K. W. DeLong, D. N. Fittinghoff, J. N. Sweetser, M. A. Krumbügel, B. A. Richman, and D. J. Kane, Rev. Sci. Instrum. **68**, 3277 (1997).
[62] S. M. Hankin, D. M. Villeneuve, P. B. Corkum, and D. M. Rayner, Phys. Rev. A **64**, 013405 (2001).
[63] M. J. DeWitt, E. Wells, and R. R. Jones, Phys. Rev. Lett. **87**, 153001 (2001).
[64] E. Wells, M. J. DeWitt, and R. R. Jones, Phys. Rev. A **66**, 013409 (2002).
[65] C. Guo, M. Li, J. P. Nibarger, and G. N. Gibson, Phys. Rev. A **58**, R4271 (1998).
[66] P. Hansch, M. A. Walker, and L. D. Van Woerkom, Phys. Rev. A **54**, R2559 (1996).
[67] G. Herzberg, *Electronic Spectra and Electronic Structure of Polyatomic Molecules* (Van Nostrand, New York, 1966).
[68] L. R. H. Scharpen, J. S. Muenter, and V. W. Laurie, J. Chem. Phys. **53**, 2513 (1970).
[69] P. R. Bevington and D. K. Robinson, *Data Reduction and Error Analysis for the Physical Sciences*, 3rd ed. (McGraw-Hill, New York, 2003).
[70] K. B. Anderson and J. A. Conder, Energy Fuels **25**, 1578 (2011).
[71] J. C. Lagarias, J. A. Reeds, M. H. Wright, and P. E. Wright, SIAM J. Optim. **9**, 112 (1998).
[72] H. Ohmura and M. Tachiya, Phys. Rev. A **77**, 023408 (2008).
[73] T. H. Dunning, Jr., J. Chem. Phys. **90**, 1007 (1989).
[74] P. Krause and H. Bernhard Schlegel, J. Chem. Phys. **141**, 174104 (2014).
[75] C. Adamo and V. Barone, J. Chem. Phys. **110**, 6158 (1999).
[76] J. P. Perdew, K. Burke, and M. Ernzerhof, Phys. Rev. Lett. **77**, 3865 (1996).
[77] E. Livshits and R. Baer, Phys. Chem. Chem. Phys. **9**, 2932 (2007).
[78] T. Stein, L. Kronik, and R. Baer, J. Chem. Phys. **131**, 244119 (2009).
[79] R. Baer, E. Livshits, and U. Salzner, Annu. Rev. Phys. Chem. **61**, 85 (2010).
[80] A. Karolewski, L. Kronik, and S. Kümmel, J. Chem. Phys. **138**, 204115 (2013).
[81] J. I. Fuks, P. Elliott, A. Rubio, and N. T. Maitra, J. Phys. Chem. Lett. **4**, 735 (2013).
[82] J. I. Fuks, K. Luo, E. D. Sandoval, and N. T. Maitra, Phys. Rev. Lett. **114**, 183002 (2015).
[83] C. A. Ullrich, J. Mol. Struct.: THEOCHEM **501-502**, 315 (2000).
[84] K. Doblhoff-Dier, M. Kitzler, and S. Gräfe, Phys. Rev. A **94**, 013405 (2016).